Journal of Alloys and Compounds 487 (2009) 499–503

Contents lists available at ScienceDirect

Journal of Alloys and Compounds

journal homepage: www.elsevier.com/locate/jallcom

A thermal model for laser interaction with thick dielectric film on metallic substrate: Application to Ca–P layer on Ti alloy

Sameer R. Paital, Narendra B. Dahotre*

Laboratory for Laser Materials Synthesis and Fabrication, Department of Materials Science and Engineering, The University of Tennessee, Knoxville, TN 37996, USA

ARTICLE INFO

Article history:
Received 11 July 2009
Received in revised form 21 July 2009
Accepted 25 July 2009
Available online 5 August 2009

Keywords:
Laser
Thermal model
Calcium phosphate tribasic
Bioceramics
Phase transformations

ABSTRACT

Ca–P coatings on Ti–6Al–4V substrates were synthesized using a direct pulsed Nd:YAG laser writing technique. The phase and morphological evolutions within the coatings as a function of laser processing parameters were evaluated using X-ray diffraction and scanning electron microscopy techniques. A three dimensional modeling based on COMSOL's™ Multiphysics was adopted to understand the temperature evolution and corresponding cooling rate as a function of laser processing parameters. The temperature evolutions and cooling rate estimated from the model, satisfactorily explained the variation in phases and melt depth with varying pulse frequency of the laser beam.

1. Introduction

Titanium-based alloys owing to their excellent mechanical properties, corrosion resistance and biocompatibility are most commonly used for load bearing implant applications, such as hip joint prosthesis, knee joint prosthesis and dental implants. However, these bioinert materials when placed inside a human body elicit minimal interaction with the surrounding tissues and thereby induce the formation of a fibrous capsule at the interface [1,2]. Hence, to improve the reaction between the implant and surrounding tissue, bioresorbable materials such as tricalcium phosphate (α-TCP, $Ca_3(PO_4)_2$) [2] and bioactive materials such as hydroxyapatite [$Ca_{10}(OH)_2(PO_4)_6$] (HA) [3], calcium phosphate tribasic [$Ca_5(OH)(PO_4)_3$] [4], and bioglass [5] are most commonly used as coatings on Ti-based alloys. These bioceramics react with the surrounding tissue and thereby provide a strong chemical bonding between the implant and the remodeling bone. Further, coatings of these bioceramics on Ti-based alloys provide the appropriate surface chemistry for tissue compatibility without altering the bulk mechanical properties of the material.

The several coating techniques that can be used to achieve Ca–P coatings on Ti-based alloys are plasma spray deposition [6], pulsed laser physical vapor deposition [7], ion beam assisted deposition [8], magnetron sputtering [9], sol–gel-based coatings [10] and electrodeposition [11]. Most of the above coatings however suffer from certain drawbacks such as poor adherence of the coating to the substrate material, lack of uniformity in the coating and absence of textures or topographical cues [12,13]. Hence, in the present work, a laser-based direct writing technique to synthesize Ca–P coatings on titanium alloys is introduced. In this approach, by proper selection of laser processing parameters both the precursor (calcium phosphate tribasic) and a part of the substrate material (Ti–6Al–4V) can undergo rapid melting and thereby a chemical and microstructural bonding can be achieved at the interface. Further, by controlling the pulse frequency, the input laser energy and thereby the phase and morphological evolutions within the coatings can also be modulated. Finally, a three dimensional thermal model based on COMSOL's™ Multiphysics is adopted to understand the phase transformations with varying laser processing parameters.

2. Materials and methods

Ti–6Al–4V substrate coupons (100 mm × 50 mm × 3 mm) cut from the rolled sheets were polished using 30 μm grit SiC emery paper followed by rinsing with acetone. Calcium phosphate tribasic ($Ca_5(OH)(PO_4)_3$) powder (Fisher Scientific, USA) was used as the precursor material. This precursor powder had a spherical morphology with a unimodal distribution in the range of 10–30 μm. The precursor was mixed in a water-based organic solvent LISI W 15853 (Warren Paint and Color Company, Nashville, TN, USA) and sprayed onto the substrate coupons using an air pressurized spray gun. This green body was air dried to remove the moisture and a uniform thickness of 40 μm was maintained for all precoating precursor deposits. The samples were then scanned using a 400 W average power, JK701 model pulsed Nd:YAG laser to obtain the coating. The additional details related to the laser processing technique are available in the previously published article [4]. The processing parameters used for the above process are listed in Table 1.

Phase evolutions within the coatings were studied using a Philips Norelco X-ray diffractometer (XRD) with Cu-Kα radiation of wavelength 1.5418 Å. The system was

* Corresponding author. Tel.: +1 865 974 3609; fax: +1 865 974 4115.
E-mail address: ndahotre@utk.edu (N.B. Dahotre).

0925-8388/$ – see front matter © 2009 Elsevier B.V. All rights reserved.
doi:10.1016/j.jallcom.2009.07.162

Table 1
Laser parameters used for the experiment.

Pulse duration	0.5 ms
Energy of a single pulse (e)	4 J
Pulse frequency	10, 20, 30, 40 Hz
Input laser energy (E)	4, 7.92, 10.48, 13.8 J
Laser scan speed	36 cm/min
Focus position	0.8 mm above the surface of the sample
Laser spot diameter on the surface	900 μm
Pulse shape	Rectangular

operated at 20 kV and 10 mA in a 2θ range of 20–100° using a step size of 0.02° and count time of 1 s. The observations for microstructure evolution and depth of heat-affected zone due to laser direct writing were conducted across the cross-section of samples. The samples were chosen from the center of the coated plate and were sectioned using a low speed diamond cutter (Buehler) so as to have at least three overlapping laser tracks. The samples in cross-section were then prepared by polishing with emery papers of grit sizes ranging from 200 to 1000 μm in succession followed by disc polishing with colloidal silica of 0.3 and 0.05 μm to get a mirror finished surface. The polished samples were then cleaned with acetone and etched with 5 vol% HF, 3 vol% HNO_3, and 92 vol% H_2O for 10–20 s by immersion etching to reveal the microstructural features. A Jeol scanning electron microscope (SEM) coupled with EDS (energy dispersive spectrometer) was used to characterize for the microstructural and elemental analysis at different locations of the coatings.

A three dimensional thermal model based on COMSOL's™ Multiphysics was adopted in the present work to predict thermal parameters (temperature evolution and cooling rate) which in turn influence the phase evolutions within the coatings. The composite nature of the material system (coating + substrate), temperature dependent thermophysical properties, conduction, convection and radiation dependent heat transfer during laser processing were taken into account. Apart from this, various other assumptions and dimensions of the geometry considered in the present work are based on the earlier work by the group [14]. The residence time (time required to travel the diameter of the beam), the on and off period during each residence time and the peak power (input power density in W/m^2) during the laser on periods were employed for thermal analysis. The residence time (t) of the laser beam for a pulsed Nd:YAG laser can be calculated as per the following equation:

$$t = \frac{D}{V} \tag{1}$$

Here, D is the laser beam diameter on the surface and V is the laser scan speed. The total on time (t_{on}) and off time (t_{off}) of the laser beam within the residence time is therefore given as:

$$t_{on} = \frac{f \times w \times D}{V} \tag{2}$$

$$t_{off} = t - t_{on} \tag{3}$$

Here, f is the laser frequency and w is the pulse duration of laser beam. The input power density or the intensity (I) of the laser beam used in the model was calculated as per the following equation:

$$I = \frac{D \times E \times f}{V \times \Phi \times w} \tag{4}$$

Here, E is the input energy and Φ the cross-sectional area of the laser beam. As, with increasing pulse frequency, the number of pulses within the residence time of the laser beam increases, the input energy E of the laser beam contributed by these pulses is given by the following equation [15]:

$$E = \left[\sum_{n}^{N_d} \frac{D - (n-1)b}{D} \right] e \tag{5}$$

Here, N_d is the total number of pulses that can be obtained dividing the total on time of the laser beam (Table 2) by the pulse duration of laser beam, n corresponds to each of these pulses and is taken as $n = 1, 2, 3, \ldots N_d$ and e is the energy from a single pulse. The distance traveled by the laser between two successive pulses is b and calculated as follows:

$$b = (1 - X) \times D \tag{6}$$

Here, X is the spot overlap of the laser beam and can be calculated from the following equation:

$$X = 1 - \frac{V}{fD} \tag{7}$$

The Fourier's second law of heat transfer (Eq. (8)) in COMSOL's™ heat transfer mode was used to model the energy transfer from the laser beam to the precursor during coating:

$$\frac{\partial T(x,y,z,t)}{\partial t} = \alpha \left[\frac{\partial^2 T(x,t)}{\partial x^2} + \frac{\partial^2 T(y,t)}{\partial y^2} + \frac{\partial^2 T(z,t)}{\partial z^2} \right] \tag{8}$$

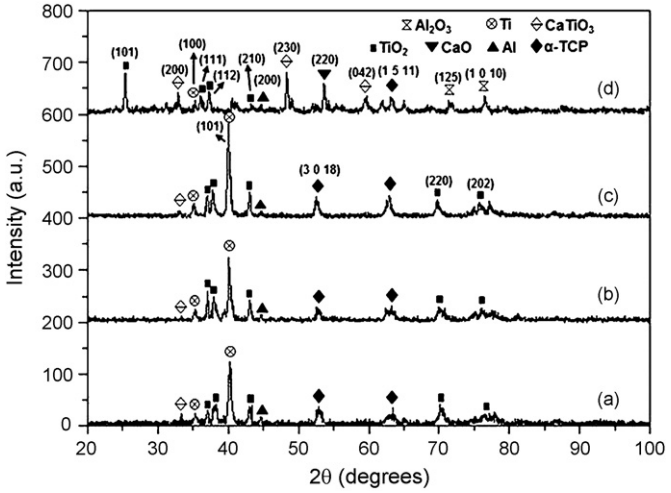

Fig. 1. XRD patterns of the samples processed at varying laser pulse frequency of (a) 10 Hz, (b) 20 Hz, (c) 30 Hz and (d) 40 Hz.

Here, α is the thermal diffusivity and is equal to $K/\rho C_p$, K is the thermal conductivity, C_p is the specific heat, and ρ is the density (precursor = 3156 kg/m^3 [16] and substrate = 4420 kg/m^3 [17]) of the material. At time $t = 0$ the initial temperature $T = T_0 = 298$ K was used in the model. For improved accuracy of temperature and cooling rate evolution, variations in specific heat and thermal conductivity of the material as a function of temperature were incorporated into the model [16,18].

The equation used to model the balance between the absorbed laser energy and radiation loss at the surface is given as:

$$-K \left[\frac{\partial T(x,t)}{\partial x} + \frac{\partial T(y,t)}{\partial y} + \frac{\partial T(0,t)}{\partial z} \right] = \delta AI - \varepsilon\sigma[T(x,y,0,t)^4 - T_0^4] \tag{9}$$

$\delta = 1$ for $0 \le t \le t_{on}$
$\delta = 0$ for $t > t_{on}$

Here, A is the absorptivity of the material and is taken as 0.1 [14,19], ε is the emmisivity of the material, and σ is the Stefan–Boltzmann constant. The emmisivity of calcium phosphate tribasic when exposed to 1064 nm wavelength laser beam is not available in the open literature. Hence, in the present model only the absorptivity was considered and attempts are being made for *in situ* emmisivity measurements under laser processing conditions similar to the ones employed in the present study and they will be incorporated in future calculations.

The convection at the bottom surface of the sample during laser processing was also incorporated into the model and is given by the following equation:

$$-K \left[\frac{\partial T(x,t)}{\partial x} + \frac{\partial T(y,t)}{\partial y} + \frac{\partial T(L,t)}{\partial z} \right] = h[T(x,y,L,t) - T_0] \tag{10}$$

Here, h is the convective heat transfer coefficient (W/m^2 K), incorporated as function of temperature [20], and L the thickness of sample (0.04 mm for the precursor, Ca–P + 3 mm for the substrate, Ti–6Al–4V). The solutions of the above three equations were obtained by using the heat transfer module of COMSOL's™ Multiphysics package, and the results were discussed in later part of the paper.

3. Results and discussions

As the interaction of the laser beam with the precursor and substrate material is an energy intensive process the precursor $Ca_5(OH)(PO_4)_3$ is not expected to be retained and hence X-ray diffraction studies were carried out to observe the change in phases. The overlap of XRD patterns of the coatings processed at varying laser frequencies are represented in Fig. 1. It can be observed (Fig. 1a–c) that there is no change in the types of phases evolved when the pulse frequency is varied from 10 to 30 Hz and α-TCP, TiO_2, Ti, $CaTiO_3$, and Al are the major phases within the coatings. Nevertheless, additional phases such as CaO and Al_2O_3 along with the above phases are observed (Fig. 1d) as the laser pulse frequency is increased to 40 Hz. From the peak intensities it can be realized that, although the phase constituents within the coatings are same for 10, 20 and 30 Hz there is a variation in the amounts of these phases with varying pulse frequency. The relative amounts of

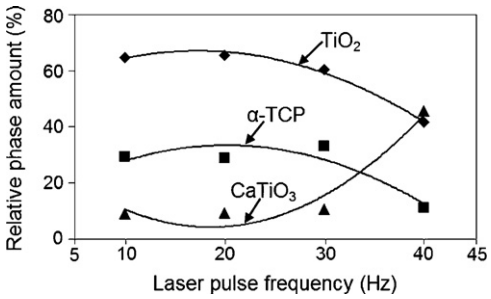

Fig. 2. Relative phase fractions as a function of laser pulse frequency.

phases of interest with regard to bio-application (α-TCP, TiO_2, and, $CaTiO_3$) were semi-quantitatively calculated as per the following equation [21]:

$$\%I = \frac{I_i}{\sum_1^3 I_i} \times 100 \quad (11)$$

Here, I_i is the integrated intensity of the phase in concern normalized to the integrated intensity of the Ti peaks and $\sum_1^3 I_i$ is the sum of these integrated intensities for the three phases. The results as illustrated in Fig. 2 show a decrease in the relative amounts of TiO_2 and α-TCP phase and an increase in the relative amount of $CaTiO_3$ phase with increasing pulse frequency. The kinetics and stability of these phase transformations and the relative amounts of these phases was understood from the temperature evolutions and cooling rate estimations during processing of the composite system (coating + substrate) made by using the thermal model as explained in the earlier section.

The temperature evolutions as a function of depth for all laser frequencies employed in the present work and corresponding cooling rates during processing of the composite system are represented in Fig. 3. It can be observed (Fig. 3) that within the frequency range of 10–30 Hz the temperatures at the surface (2100, 2680, 3688 K) and corresponding substrate-coating interface (1850, 2400, 3200 K) were high enough to melt the precursor calcium phosphate tribasic (melting point of 1843 K [16]) and substrate Ti–6Al–4V (melting point of 1800 K [18]) respectively. Hence, the dissociation products (α-TCP, TiO_2, and $CaTiO_3$,) are a result of direct interaction between the calcium phosphate tribasic and the substrate and their oxidation in the melt pool as per the following possible equations [4,22,23]:

$$2[Ca_5(OH)(PO_4)_3] + TiO_2 \rightarrow CaTiO_3 + 3\alpha\text{-}TCP + H_2O(g)\uparrow \quad (1)$$

$$\alpha\text{-}TCP + TiO_2 \rightarrow CaTiO_3 + \alpha\text{-}Ca_2P_2O_7 \quad (2)$$

$$\alpha\text{-}Ca_2P_2O_7 + Ti \rightarrow CaTiO_3 + CaO + P_2O_3(g)\uparrow \quad (3)$$

Once CaO is formed, it can easily react with TiO_2 to form $CaTiO_3$ as per the following equation:

$$CaO + TiO_2 \rightarrow CaTiO_3 \quad (4)$$

Further, as the laser pulse frequency is increased to 40 Hz the temperature at the surface (4800 K) and at substrate coating interface (4150 K) was sufficient enough to evaporate a major portion

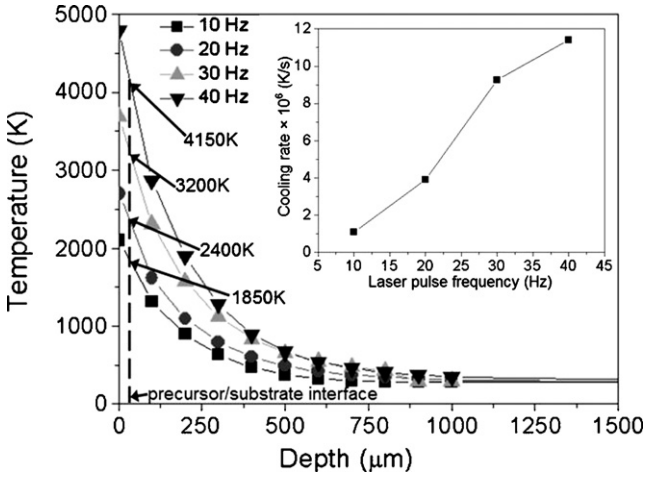

Fig. 3. Temperature evolution as a function of depth for samples processed at varying laser pulse frequency and the inset showing the cooling rate for all laser pulse frequencies.

of the precursor (boiling point of 3500 K [16]) and substrate (boiling point of 3315 K [18]) material. Hence a severe oxidation of the substrate material has taken place resulting in the presence of additional oxidation products such as Al_2O_3 as observed in the XRD (Fig. 1). Although the temperature at surface reaches as high as 3688 K for 30 Hz there is no presence of CaO (melting point of 2843 K and boiling point of 3171 K) [14] in the XRD (Fig. 1) unlike its presence in 40 Hz pulsing. This is attributed to the fact that as the cooling rates (inset in Fig. 3) for lower frequencies were relatively lower (<9.25×10^6 K/s) compared to the cooling rate of 40 Hz (11.4×10^6 K/s), there was enough time for most of CaO formed in the melt pool to evaporate and remaining to involve in formation of $CaTiO_3$ as per reaction (4). On the contrary, the associated very high cooling rate for 40 Hz pulsing resulted in solidifying some of the CaO in the matrix along with formation of $CaTiO_3$ through reaction with CaO. Hence, there was an increase in the relative amount of $CaTiO_3$ phase and decrease in the TiO_2 phase with increasing laser pulse frequency (Fig. 2).

Microstructure and depth of melt zone across the cross-section for the coated surfaces were observed using a SEM. Since, there was no change in phase evolution for the samples processed at 10, 20, and 30 Hz, for comparison purpose, microstructural evolution and depth of melt zone across the cross-section were presented for only the samples processed at 20 and 40 Hz (Fig. 4). For the sample processed at 20 Hz the geometry of the textured topography is clearly visible and the depth of melt is approximately 220 μm (Fig. 4a). A higher magnification SEM image of the coating area, presented as an inset in Fig. 4a clearly demonstrated the rapid solidification of the precursor material to form dendrite like structures. The EDS spectra obtained from a random location in this area indicated the strong presence of Ca, P, Ti, Al, V and O peaks (inset in Fig. 4a). The presence of Ti, Al and V atoms within the coating was due to the fact that a certain amount of dilution has taken place as a part of the substrate material was also melted during this process. Further, as

Table 2
Variations in total on time, total off time, melt depth and experimental laser fluence with varying pulse frequency and the theoretical fluence for evaporation of calcium phosphate tribasic.

Laser pulse frequency (Hz)	Total on time (μs)	Total off time (ms)	Melt depth (μm)	Experimental laser fluence × 10^6 (J/kg)	Theoretical fluence for evaporation × 10^6 (J/kg)
10	750	149.250	300	6.6	
20	1500	148.500	220	17.7	
30	2250	147.750	140	37.0	4.5
40	3000	147.000	80	85.1	

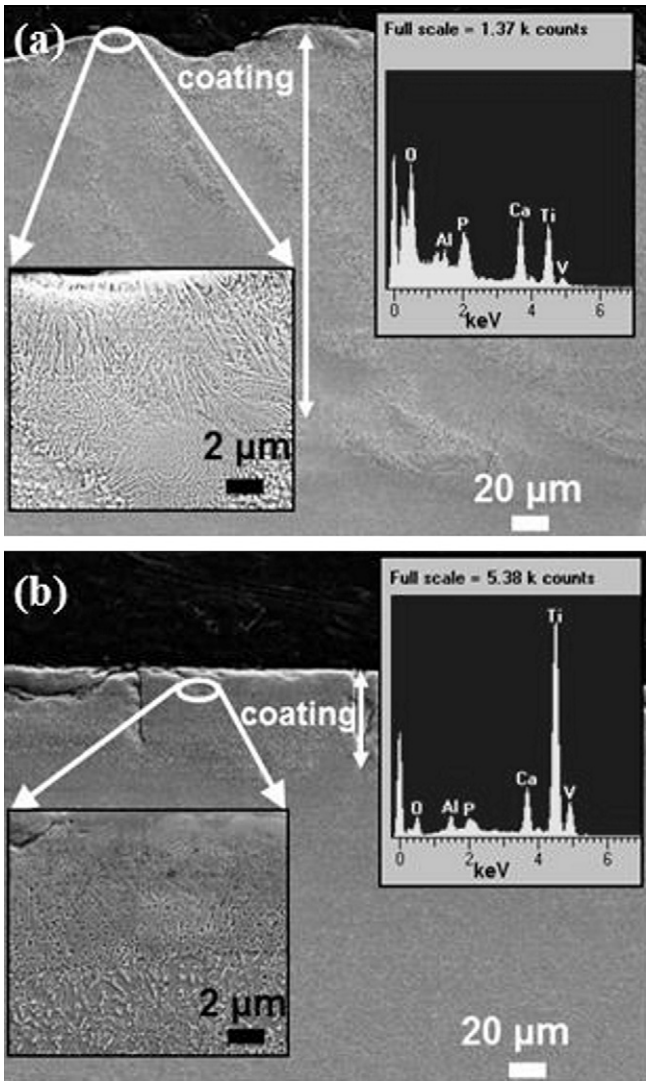

Fig. 4. SEM image and the corresponding EDS spectra for the sample processed at (a) 20 Hz and (b) 40 Hz.

the processing was carried out in an ambient atmosphere and temperature developed at the surface was very high (>2500 K, Fig. 3), a part of the precursor and substrate material may have oxidized for the presence of O peak. For samples processed at 40 Hz, the surface is less rough (Fig. 4b) compared to the sample processed at 20 Hz (Fig. 4a) and the depth of melt zone is approximately 80 μm (Fig. 4b). The less surface roughness in 40 Hz sample is attributed to the increased pulse overlap with increasing pulse frequency [24]. In addition EDS (inset in Fig. 4b) indicate that 40 Hz sample has very weak peak of Ca and P from coated region. Such weak peaks of Ca and P along with lower melt depth in 40 Hz sample compared to 20 Hz sample even with higher input laser energy (Table 1) is explained in the following section.

The correlation between melt depth and pulse frequency strongly depends upon the input energy and corresponding thermal parameters (temperature and cooling rate) and physical conditions generated and prevailed during processing. Depending upon the input energy, the temperature will rise to melt or vaporize the material. Especially, during laser material processing, presence of vapor over the surface of sample strongly influences the transfer (coupling) of the incoming laser beam energy and accordingly affects the chemical and physical nature of modified surface region. The theoretical energy $Q_{\text{theoretical}}$ required to vaporize a unit mass of material can be calculated by the following equation:

$$Q_{\text{theoretical}} = \int_{298}^{T_m} (C_p\,\mathrm{d}T) + \Delta H_m + \int_{T_m}^{T_v} (C_p\,\mathrm{d}T) + \Delta H_v \tag{12}$$

Here, C_p is the specific heat of calcium phosphate tribasic and its variation with temperature is taken as $C_p = 201.68T^{0.245}$ J/kg K[10], ΔH_m and ΔH_v are the latent heat of melting and latent heat of vaporization for calcium phosphate tribasic and are taken as 15.5 kJ/mol [16], and 458.24 kJ/mol [16] respectively. With increase in pulse frequency, the number of pulses within a single beam area is increased and therefore the experimental energy $Q_{\text{experimental}}$ delivered per unit mass can be calculated as per the following equation:

$$Q_{\text{experimental}} = \frac{4E}{\rho_{\text{Ca-P}}\pi D^2 l} \tag{13}$$

Here, $\rho_{\text{Ca-P}}$ is the density of calcium phosphate tribasic (3156 kg/m^3 [16]) and l the melt depth. The theoretical and experimental energy obtained from these calculations and melt depths measured in the cross-section are listed in Table 2. While the experimental laser energies for the samples processed at 10, 20 and 30 Hz are higher but less than an order of magnitude to that of the theoretical energy, the experimental energy for the sample processed at 40 Hz is approximately 2 orders of magnitude higher than the theoretical energy. Hence, a predominant amount of precursor material likely to have evaporated while processing at 40 Hz thereby resulting in a reduced melt depth as stated earlier. Further, for the sample processed at 40 Hz the total on time of the laser beam (Table 2) was sufficiently long (3000 μs) as compared to the samples processed at 10, 20 and 30 Hz, for formation of a stable plasma on the surface. Such plasma is likely to block the incoming laser beam and further reduce the melt depth. The presence of cracks (Fig. 4b) for the sample processed at 40 Hz might be due to the shock waves generated at the interface as a result of the stable plasma plume.

4. Conclusions

From the model calculations it was observed that as the laser pulse frequency is increased, the surface temperature and the cooling rate increased. This in turn resulted in a reduction of the relative phase amounts of α-TCP and TiO_2 and an increase in $CaTiO_3$ phase. Further, with increasing pulse frequency the input energy needed to vaporize a unit mass of material increases beyond the theoretical energy. This in turn resulted in evaporation of precursor material at higher laser frequencies (40 Hz). The stable plasma plume formed on the surface at such higher laser frequencies is likely to decouple the incoming laser beam and further reduce the melt depth.

References

[1] L.L. Hench, J.M. Polak, Science 295 (2002) 1014–1017.
[2] L.L. Hench, R.E. Newnham, Journal of American Ceramic Society 74 (1991) 1487–1510.
[3] H.W. Kim, Y.H. Koh, L.H. Li, S. Lee, H.E. Kim, Biomaterials 25 (2004) 2533–2538.
[4] S.R. Paital, K. Balani, A. Agarwal, N.B. Dahotre, Biomedical Materials 4 (2009) 1–10.
[5] K. Takatsuka, T. Yamamuro, T. Kitsugi, T. Nakamura, T. Shibuya, T. Goto, Journal of Applied Biomaterials 4 (2004) 317–329.
[6] Y.C. Tsui, C. Doyle, T.W. Clyne, Biomaterials 19 (1998) 2015–2029.
[7] C.K. Wang, J.H. Chern Lin, C.P. Ju, H.C. Ong, R.P.H. Chang, Biomaterials 18 (1997) 1331–1338.
[8] T. Blalock, X. Bai, A. Rabiei, Surface and Coatings Technology 201 (2007) 5850–5858.
[9] A.R. Boyd, B.J. Meenan, N.S. Leyland, Surface and Coatings Technology 200 (2006) 6002–6013.
[10] D.B. Haddow, P.F. James, R. Van Noort, Journal of Materials Science: Materials in Medicine 7 (1996) 255–260.
[11] M. Shirkhanzadeh, Journal of Materials Science Letters 10 (1991) 1415–1417.
[12] A.A. Campbell, G.E. Fryxell, J.C. Linehan, G.L. Graff, Journal of Biomedical Materials Research 32 (1996) 111–118.

[13] F.J. Gracia-Sanz, M.B. Mayor, J.L. Arias, J. Pou, B. Leon, M. Perez-Amor, Journal of Materials Science: Materials in Medicine 8 (1997) 861–865.
[14] A.K. Kurella, A.N. Samant, N.B. Dahotre, Journal of Applied Physics 105 (2009) 149131–149138.
[15] A.N. Samant, Laser Machining of Structural Ceramics: Computational and Experimental Analysis, Doctoral Dissertation, The University of Tennessee, Knoxville, 2009, p. 131.
[16] S. Dyshlovenko, B. Pateyron, L. Pawlowski, D. Murano, Surface and Coatings Technology 179 (2004) 110–117.
[17] R. Singh, A. Kurella, N.B. Dahotre, Journal of Biomaterials Applications 21 (2006) 49.
[18] M. Boivineau, C. Cagran, D. Doytier, V. Eyraud, M.-H. Nadal, B. Wilthan, G. Pottlacher, International Journal of Thermophysics 27 (2006) 507–529.
[19] O. Guillot-Noël, R. Gomez-San Roman, J. Perrière, Jörg Hermann, V. Craciun, C. Boulmer-Leborgne, P. Barboux, Journal of Applied Physics 80 (1996) 1803.
[20] F.P. Incropera, D.P. Dewitt, Fundamentals of Heat and Mass Transfer, 6th ed., John Wiley and Sons, New York, 2002, p. 543.
[21] B. Du, S.R. Paital, N.B. Dahotre, Scripta Materialia 59 (2008) 1147–1150.
[22] A. Kurella, N.B. Dahotre, Acta Biomaterialia 2 (2006) 677–683.
[23] F. Lusquiños, A. De Carlos, J. Pou, J.L. Arias, M. Boutinguiza, B. León, M. Pérez-Amor, F.C.M. Driessens, K. Hing, I. Gibson, S. Best, W. Bonfield, Journal of Biomedical Materials Research 64A (2003) 630–637.
[24] S.R. Paital, N.B. Dahotre, Wettability and kinetics of hydroxyapatite precipitation on a laser-textured Ca-P bioceramic coating, Acta Biomaterialia, (2009), doi:10.1016/j.actabio.2009.03.004.